

Stacking-dependent exciton multiplicity in WSe₂ bilayers

Zhijie Li,¹ Jonathan Förste,¹ Kenji Watanabe,² Takashi Taniguchi,³ Bernhard Urbaszek,⁴ Anvar S. Baimuratov,¹ Iann C. Gerber^{4,*}, Alexander Högele^{1,5,†} and Ismail Bilgin^{1,‡}

¹*Fakultät für Physik, Munich Quantum Center, and Center for NanoScience (CeNS),*

Ludwig-Maximilians-Universität München, Geschwister-Scholl-Platz 1, 80539 München, Germany

²*Research Center for Functional Materials, National Institute for Materials Science, 1-1 Namiki, Tsukuba 305-0044, Japan*

³*International Center for Materials Nanoarchitectonics, National Institute for Materials Science, 1-1 Namiki, Tsukuba 305-0044, Japan*

⁴*Université de Toulouse, Institut National des Sciences Appliquées (INSA)-Centre national de la recherche scientifique (CNRS)-Université Toulouse III—Paul Sabatier (UPS), Laboratoire de Physique et Chimie de Nano-Objets (LPCNO), 135 Avenue Rangueil, 31077 Toulouse, France*

⁵*Munich Center for Quantum Science and Technology (MCQST), Schellingstraße 4, 80799 München, Germany*



(Received 21 February 2022; revised 21 June 2022; accepted 22 June 2022; published 11 July 2022)

Twisted layers of atomically thin two-dimensional materials realize a broad range of quantum materials with engineered optical and transport phenomena arising from spin and valley degrees of freedom and strong electron correlations in hybridized interlayer bands. Here, we report on experimental and theoretical studies of WSe₂ homobilayers obtained in two stable configurations of *2H* (60° twist) and *3R* (0° twist) stackings by controlled chemical vapor synthesis of high-quality large-area crystals. Using optical absorption and photoluminescence (PL) spectroscopy at cryogenic temperatures, we uncover marked differences in the optical characteristics of *2H* and *3R* bilayer WSe₂ which we explain on the basis of beyond-density functional theory calculations. Our results highlight the role of layer stacking for the spectral multiplicity of momentum-direct intralayer exciton transitions in absorption and relate the multiplicity of phonon sidebands in the PL to momentum-indirect excitons with different spin valley and layer character. Our comprehensive study generalizes to other layered homobilayer and heterobilayer semiconductor systems and highlights the role of crystal symmetry and stacking for interlayer hybrid states.

DOI: [10.1103/PhysRevB.106.045411](https://doi.org/10.1103/PhysRevB.106.045411)

I. INTRODUCTION

The optical properties of transition metal dichalcogenide (TMD) semiconductors are governed by excitons in different spin, valley, and layer configurations [1,2]. Among possible realizations of TMD systems, heterobilayers and homobilayers stand out as hosts of excitons with layer-indirect character. Initial studies of homobilayers were limited to natural *2H* layer stacking with antiparallel alignment or 60° twist angle [3–5], extracted by exfoliation from native crystals and structurally different from *3R* stacking with parallel alignment or 0° twist. Recently, variations of the twist angle in WSe₂ bilayers (BLs) away from *2H* and *3R* stackings revealed unique phenomena ranging from correlated electronic phases [6] to moiré exciton physics [7,8] with angle-controlled exciton valley coherence and dynamics [8–10], Coulomb correlations in effectively flat moiré exciton bands [11], or optical nonlinearities [12].

A particularly attractive feature of interlayer excitons in related homobilayer systems is provided by the permanent dipole moment of layer-indirect excitons [13–15] which

promotes exciton-exciton dipolar interactions, allows employing electric fields to tune the optical properties via the Stark effect [10,16–21] or implementing exciton trapping and routing [22]. The electrostatic dipole moment depends on the degree of exciton layer delocalization, which in turn is sensitive to the interlayer coupling and thus to the stacking order, as was shown recently by optical absorption for *2H*- and *3R*-MoS₂ BLs for transitions involving momentum-direct *KK* excitons [23,24]. In contrast to absorption probing zero-momentum exciton transitions, the photoluminescence (PL) of BLs is dominated by momentum-indirect excitons [25,26] via luminescence phonon sidebands [27–29] which exhibit linear energy shifts in perpendicular electric fields according to the Stark effect [10,16,20,21]. The most recent observation of two different slopes in the energy dispersion of phonon sideband emission from *2H*-WSe₂ BLs in an electric field [20,21] indicates the presence of two degrees of electron-hole layer separation, with respective dipole moments attributed to excitons in distinct *QK* and *QΓ* reservoirs [20,21]. Experiments employing strain tuning [30] and magnetic fields [28], on the other hand, suggest that the PL sidebands stem exclusively from *QK* excitons, indicating shortcomings in the present understanding of the underlying lowest-energy exciton reservoirs with finite center-of-mass momenta.

To provide comprehensive insight into the nature of exciton reservoirs in BL WSe₂ with different spin, momentum, and

*igerber@insa-toulouse.fr

†alexander.hoegle@lmu.de

‡bilgin.ismail@lmu.de

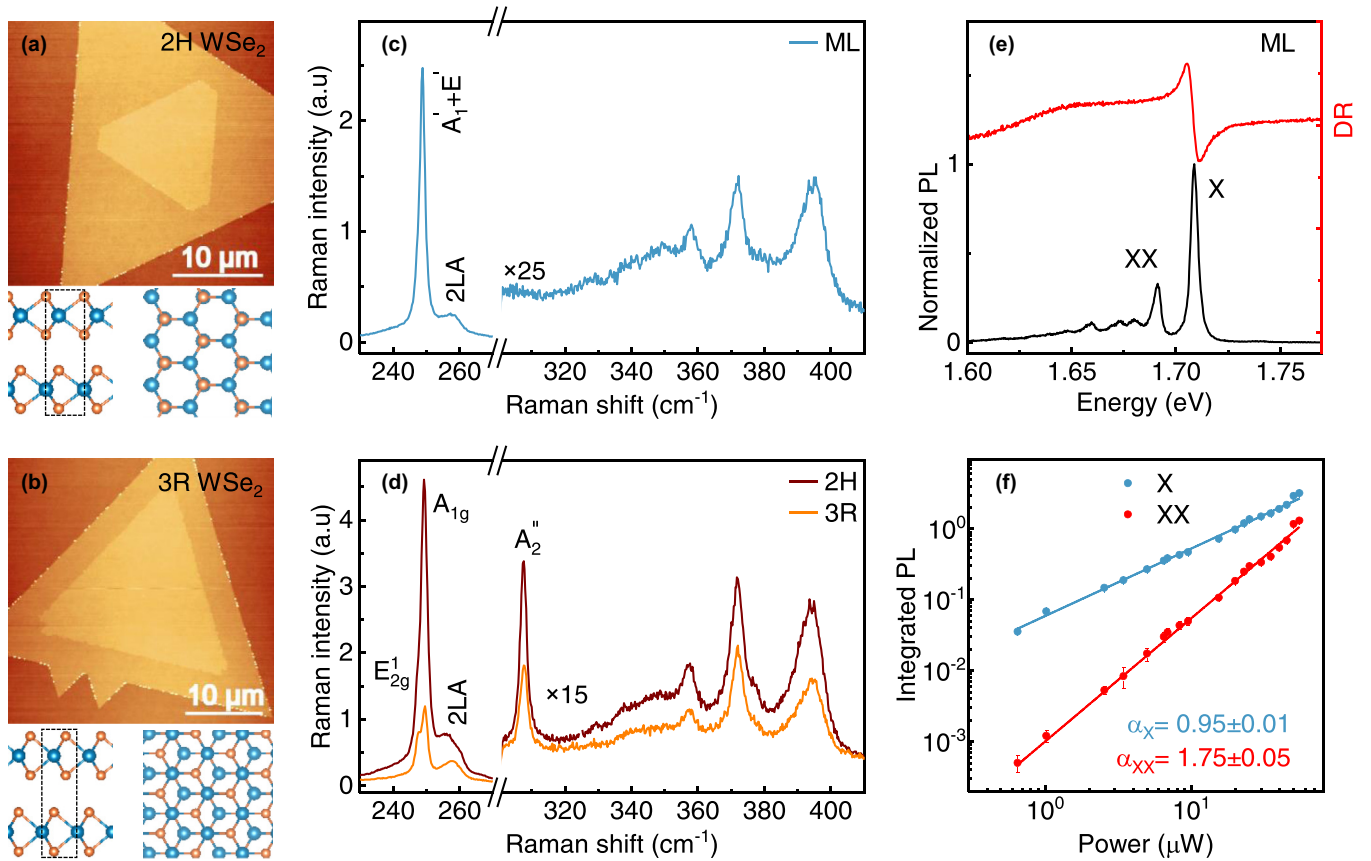


FIG. 1. Characteristics of high-quality chemical vapor deposition (CVD)-grown WSe_2 homobilayers. (a) and (b) Atomic force micrographs of $2H$ and $3R$ homobilayer WSe_2 on SiO_2/Si , respectively, with side- and top-view illustrations of the respective stacking orientations shown below (blue and orange spheres represent W and Se atoms, respectively, dashed rectangles indicate the unit cell). (c) and (d) Room-temperature Raman spectra of monolayer (ML) and bilayer (BL) WSe_2 in $2H$ and $3R$ stacking (the spectra were recorded with excitation at 532 nm and normalized to the peak intensity of the Si phonon mode at 520 cm^{-1} ; note that the intensity of higher-order Raman modes associated with multiphonon processes were scaled for increased visibility). The in-plane and out-of-plane phonon modes, E' and A'_1 , are degenerate in the ML but split by 2 cm^{-1} in both $2H$ and $3R$ homobilayer WSe_2 . (e) Normalized photoluminescence (black) and differential reflectivity (red) spectra at 3.2 K , recorded in the ML region of hexagonal boron nitride (hBN)-encapsulated BL WSe_2 crystals. The ML exciton (X) and biexciton (XX) peaks exhibit characteristic linear and superlinear scaling of the integrated photoluminescence (PL) intensity as a function of the excitation power, as evident from data and respective power law fits $I_{\text{PL}} \propto P^\alpha$ shown by solid lines in (f).

layer character, we performed experimental and theoretical studies of $2H$ and $3R$ stackings with contrasting spectroscopic responses. To access spectrally narrow exciton transitions, we synthesized high-quality WSe_2 crystals by chemical vapor deposition (CVD), yielding $2H$ and $3R$ as two stable limits of relative layer orientation. As opposed to BL crystals of MoS_2 [23,24,31] and WS_2 [32,33] synthesized by CVD, studies of WSe_2 BLs in $3R$ stacking have remained elusive due to the challenge of perfect layer alignment. The only realization of nominal zero-angle twist so far has been obtained from exfoliation stacking [10], which can only approximate the ideal $3R$ layer order inherent to CVD growth. Moreover, the spectral features of BLs aligned near zero twist can be compromised by marginal-angle reconstruction [8,34–36] with interfacial ferroelectricity effects [37], as observed recently for reconstructed homobilayers of hexagonal boron nitride (hBN) [38–40] and TMDs [41,42].

In the following, we present a comprehensive study of excitons in $2H$ - and $3R$ - WSe_2 BLs, performed with cryogenic

optical spectroscopy on CVD-synthesized high-quality crystals. With a set of complementary spectroscopy techniques, we identify contrasting responses of $2H$ and $3R$ BL configurations and observe rich exciton multiplicity in the $3R$ case. We relate the differences between the optical spectra of $2H$ and $3R$ BL stackings to the nature of excitons in different spin, valley, and layer configurations. Our interpretation is based on first-principles calculations of the band structure, optical absorption and exciton g factors. Theory analysis shows that, in contrast to $2H$ stacking, the top and bottom layers in $3R$ stacking differ in their band structure and exhibit different optical bandgaps. This insight resolves the recent puzzle of two distinct intralayer KK exciton transitions observed in absorption on nearly aligned WSe_2 BLs [10]. Moreover, our theoretical analysis highlights the multiplicity and degree of layer delocalization for interlayer excitons in both $2H$ and $3R$ stackings, thus providing an intuitive explanation for different electrostatic dipole moments of QK excitons without the requirement of involving $Q\Gamma$ states [20,21].

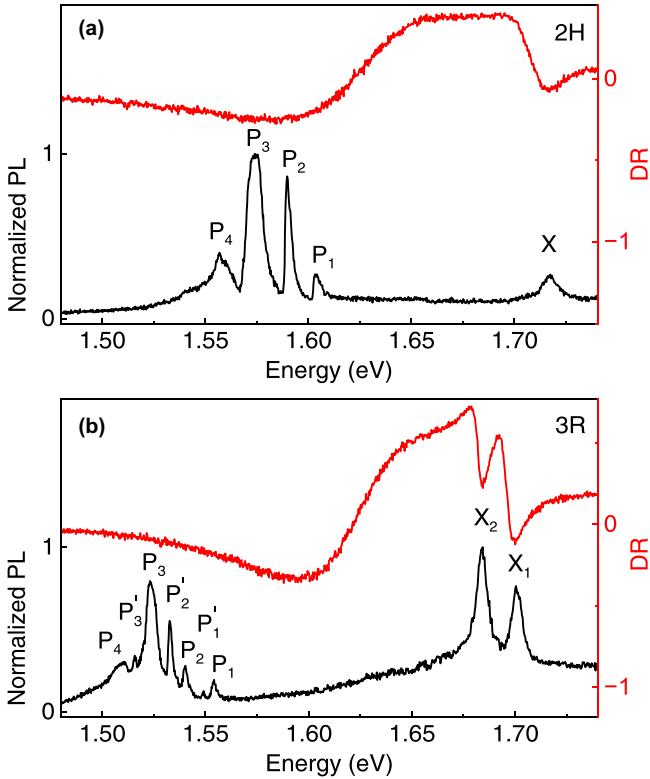


FIG. 2. Cryogenic spectroscopy of $2H$ - and $3R$ - WSe_2 homobilayers. (a) and (b) Normalized photoluminescence (PL, black) and differential reflectivity (DR, red) spectra of $2H$ - and $3R$ - WSe_2 at 3.2 K. In contrast to $2H$ with only one resonance of the fundamental exciton X , the spectra of $3R$ exhibit two exciton peaks X_1 and X_2 with a splitting of 17 meV in both PL and DR. Moreover, the series of phonon sideband PL peaks P_1 – P_4 in $2H$ redshifts by 50 meV in $3R$ and features additional peaks P'_1 – P'_3 . The contrast change in DR between the phonon sideband groups and the main exciton resonances are presumably due to phonon-assisted excitation of momentum-indirect states.

II. RESULTS AND DISCUSSION

WSe_2 BL crystals in $2H$ and $3R$ stacking were obtained from CVD synthesis. Atomic force micrographs (AFMs) in Figs. 1(a) and 1(b) show respective WSe_2 crystals with monolayer (ML) and BL regions in $2H$ and $3R$ configurations with 60° and 0° rotational alignment of the two WSe_2 MLs, as can be deduced directly from the edges of CVD flakes with the same edge termination. The corresponding atomic registries are illustrated in the bottom panels of Figs. 1(a) and 1(b), showing side (left) and top (right) views and the BL unit cell by dashed boxes. The $2H$ and $3R$ stacked BL configurations are the two energetically most favorable, which is the reason they are commonly observed in CVD grown samples with ML and BL regions of the same crystal [15].

Initial characterization of the two distinct crystal configurations was performed with Raman spectroscopy at ambient conditions. A typical Raman spectrum from a ML region is shown in Fig. 1(c). It features degenerate in-plane E' and out-of-plane A'_1 first-order Raman modes ~ 249 cm^{-1} , the double-resonance $2LA$ mode at 257 cm^{-1} , and a series of

multiphonon modes at 358, 372, and 395 cm^{-1} , all of which are consistent with ML features [43–48]. The degeneracy of the E' and A'_1 modes, characteristic of MLs [47,48], is lifted in the Raman spectra of both $2H$ and $3R$ BLs shown in Fig. 1(d). We determined by peak decomposition that, in both BL stackings, the respective E'_{2g} and A_{1g} modes exhibit the same frequency splitting of ~ 2 cm^{-1} due to interactions between the layers, with a factor of ~ 10 higher ratio of the E'_{2g} to A_{1g} peak intensities in the $3R$ case than $2H$. We also observe a redshift of the E'/E'_{2g} and a blueshift of the A'_1/A_{1g} modes for both stackings [49]. The peak at 308 cm^{-1} , labeled A'_2 , is absent in the ML limit but very pronounced in the Raman spectra of both $2H$ and $3R$ stackings as a hallmark of BL regions [43,46–48]. The spectra of multiphonon modes at frequencies > 350 cm^{-1} are similar in ML and BLs.

Having identified $2H$ and $3R$ BL crystals by AFM and Raman spectroscopy, we performed cryogenic micro-PL and differential reflection (DR) spectroscopy. To this end, the CVD-grown crystals were encapsulated in hBN by standard lift-off and exfoliation and transferred onto a Si/SiO₂ substrate. Typical PL and DR spectra of ML regions, recorded at 3.2 K, are shown in Fig. 1(e). Both spectra feature the resonance of the fundamental exciton transition (X) ~ 1.71 eV with a spectrally narrow full width at half maximum linewidth of 4 meV, exceeding the transform-limited linewidth of 1 meV in best hBN-encapsulated MLs obtained from native crystals [50–53] yet slightly narrower than 5.2 meV reported for CVD-grown MoS₂ ML in hBN [53]. The second pronounced peak in the PL spectrum at 1.69 eV corresponds to the biexciton (XX) emission with a characteristic 20 meV redshift [54–58] and superlinear dependence on the excitation power shown in Fig. 1(f). All main ML features in PL and DR confirm the overall high quality of our CVD-grown crystals.

The cryogenic PL and DR of BL regions with $2H$ and $3R$ stacking are shown in Figs. 2(a) and 2(b) with pronounced differences in the spectral characteristics. The $2H$ spectra in Fig. 2(a) agree with the results of previous studies on exfoliated BLs from bulk WSe_2 [10,27–30,59], with the neutral exciton resonance X at ~ 1.72 eV associated with momentum-direct transitions between conduction and valence band states at K , as well as a series of PL peaks between 1.55 and 1.61 eV we label P_1 to P_4 with increasing redshift. Consistent with the indirect bandgap of WSe_2 BL between the conduction band minima at the six inequivalent Q points of the first Brillouin zone and the valence band maximum at K [48,60], the lowest energy exciton states form as QK and $Q'K$ with finite center-of-mass momentum and characteristic phonon sideband luminescence into the peaks P_1 – P_4 [28,29]. As on ML regions, the high quality of our CVD-synthesized crystals is reflected by spectrally narrow features of BLs in both stackings.

The characteristic features of the $2H$ - WSe_2 BL are contrasted by the spectra from $3R$ stacking. First, the peak multiplicity increases in both PL and DR spectra of Fig. 2(b). We observe two distinct exciton resonances X_1 and X_2 ~ 1.70 and 1.68 eV with an energy splitting of 17 meV and spot-to-spot variations between 16 and 20 meV, which is very different from the single transition observed throughout the $2H$ stacked sample. As a second important observation, we

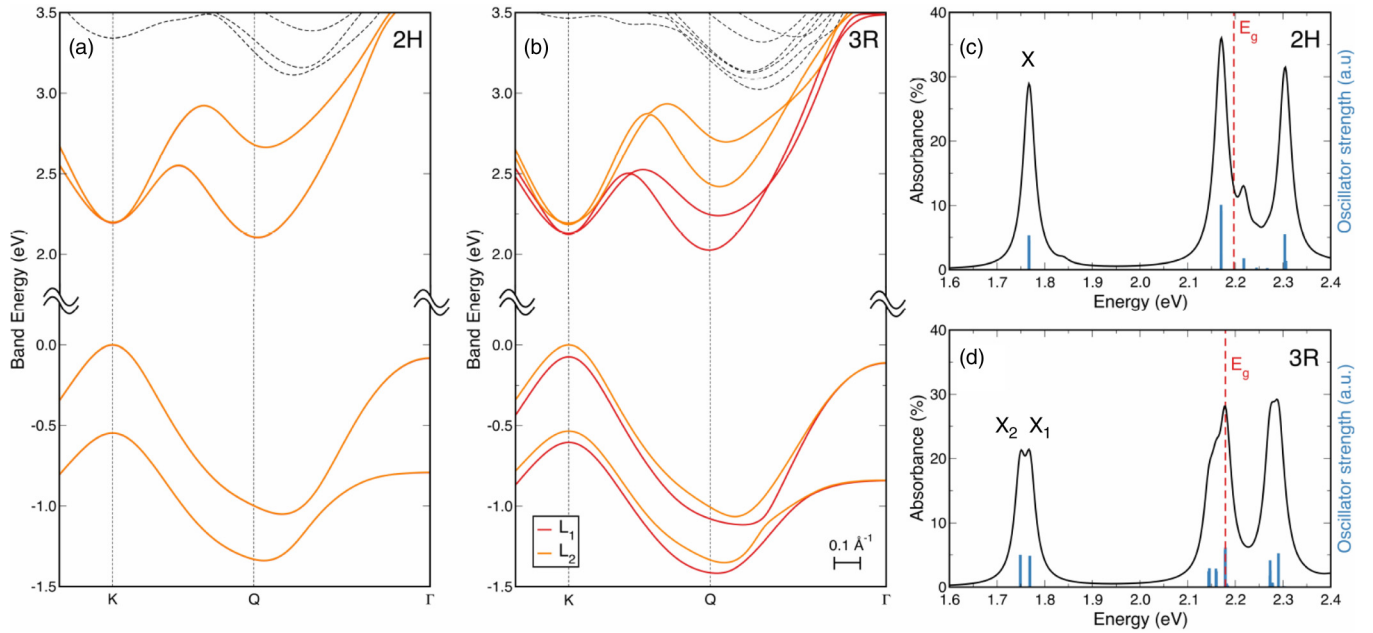


FIG. 3. Theoretical calculations for 2H- and 3R-WSe₂ homobilayers. (a) and (b) Band structure for 2H- and 3R-WSe₂ homobilayer, respectively. Red and orange colors represent the bottom and top layers, L₁ and L₂. (c) and (d) Absorption spectra (black) and oscillator strength (blue) for 2H and 3R stacking, respectively, calculated with the *GW* + Bethe-Salpeter equation (BSE) method. The dashed red lines indicate the energy gap E_g . For the absorbance in 3R, we notice globally a lifting of the exciton degeneracy, as compared with 2H. Comparison of the calculated absorption with experimental data is challenging for transitions above the A exciton, as energy splittings are masked in experiments by broad linewidths of energetically overlapping transitions.

find in the region of phonon sidebands between 1.50 and 1.55 eV three additional phonon sidebands emerging in between P₁–P₄, which we label P₁['], P₂['], and P₃[']. Moreover, we note the redshift of 16 meV from the *KK* exciton resonance X in 2H to X₁ in 3R, as well as a larger redshift to the first phonon sideband P₁ of *QK* exciton states, increasing from ~100 meV in 2H to ~150 meV in 3R as a consequence of stronger interlayer hybridization in the latter case.

To understand the increased multiplicity of exciton transitions as well as their energy shifts and splittings in 3R stacking, we carried out band structure calculations including excitonic effects via the *GW* + Bethe-Salpeter equation (BSE) approach. Our calculations, performed for WSe₂ BLs in vacuum without hBN encapsulation yield the band structure shown in Figs. 3(a) and 3(b) for 2H and 3R stacking, respectively. Due to the different atomic registries for top and bottom layers in 3R stacking, the band structure for these two layers is distinct, with different transition energies at the *K* point [61]. This is in stark contrast to 2H stacking, where both layers and their associate intralayer states are energetically degenerate. Considering hBN encapsulation in the model will result in global shifts of the spectra [62] but not impact the main difference observed between 2H and 3R, namely, the lifted exciton degeneracies in 3R.

For direct comparison of our theory with PL and DR experiments, we calculated the absorbance of momentum-direct exciton transitions for both stackings. For the 2H stacking, we found only one transition at ~1.75 eV, which corresponds to the A exciton or the X transition in the spectra of Fig. 2(a). Note that the feature at 1.85 eV with very low oscillator strength is the interlayer *KK* exciton with a much lower os-

illator strength here than in BL MoSe₂ and MoS₂ due to the larger spin-orbit coupling (SOC) in WSe₂ [9,24,63–66]. As in the experiment, we find in our calculated absorption for the 3R stacking two transitions ~1.75 eV which are separated by ~20 meV. From our calculations, we infer that the two transitions correspond to A excitons in the top and bottom layers. This insight provides a microscopic explanation for the splitting we observe for the 3R stacked sample in Fig. 2(a). Note that a similar lifting of the intralayer exciton degeneracy was anticipated for 3R-MoS₂ BLs but not clearly discernible in the experimental data [24]. The interlayer exciton feature is completely absent in 3R stacking as hybridization of electronic states at the *K* point is forbidden by symmetry [9], which is confirmed by our analysis of the atomic orbital compositions of the lowest conduction and highest valence bands obtained from density functional theory. Lower-energy momentum-indirect excitons that dominate the BL luminescence [67] via phonon-assisted emission are not captured by our absorbance calculations due to their vanishingly small oscillator strength which reflects exciton-photon momentum mismatch in direct dipolar transitions.

To complement our theory analysis of excitons in 2H- and 3R-WSe₂ BLs, we determined the exciton *g* factors from magnetoluminescence measurements and correlated them with theoretically calculated values in different spin, valley, and layer configurations [28,68]. Out-of-plane magnetic fields break the time-reversal symmetry and lift the valley degeneracy between σ^+ - and σ^- -polarized PL peaks with energies E^+ and E^- to induce a valley Zeeman splitting $\Delta = E^+ - E^- = g\mu_B B$ proportional to the exciton *g* factor, the Bohr magneton μ_B , and the magnetic field *B* [69–72]. Polarization-

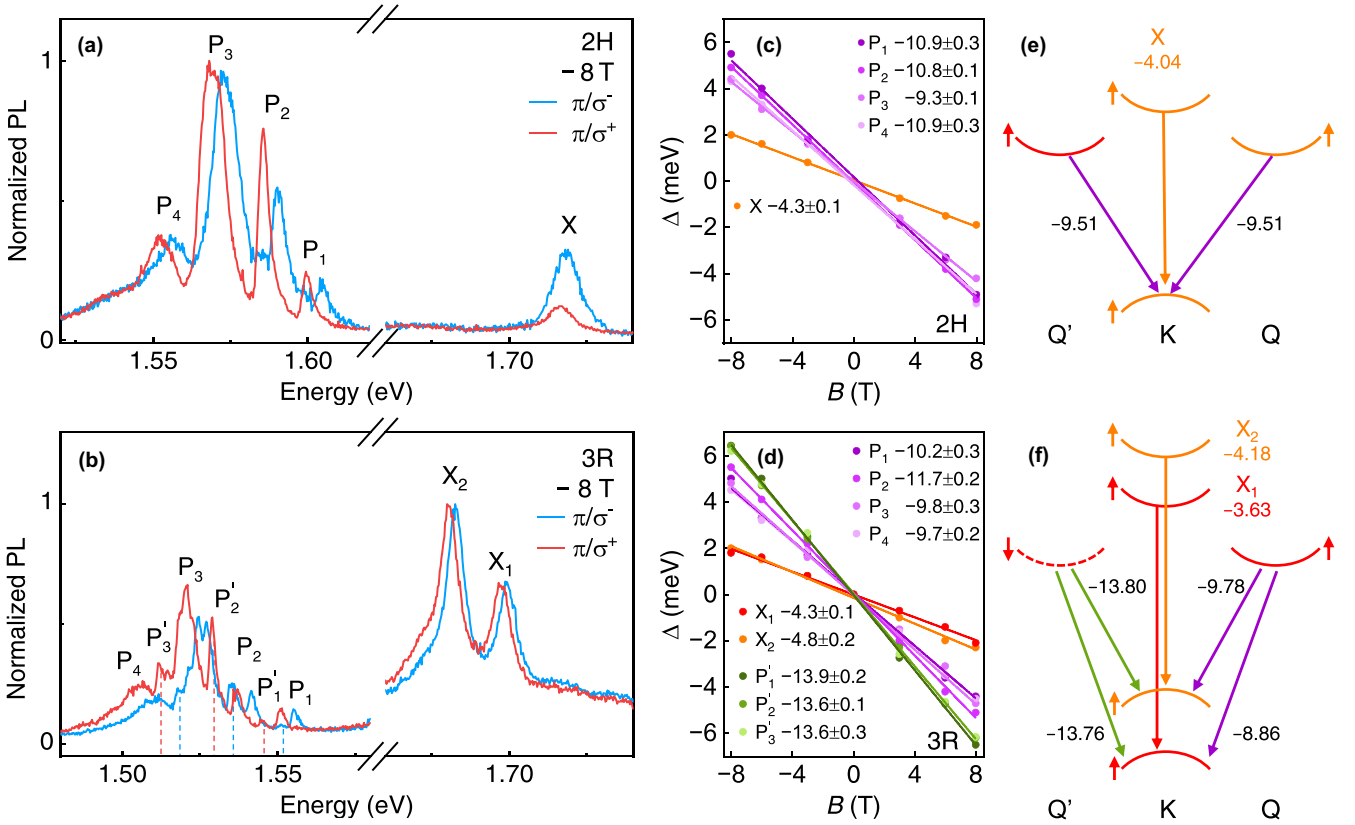


FIG. 4. Magneto-optics of 2H- and 3R-WSe₂ homobilayers in experiment and theory. (a) and (b) Photoluminescence spectra of 2H- and 3R-WSe₂ in a magnetic field of -8 T recorded with σ^+ (red) and σ^- (blue) polarized detection under linearly polarized excitation (π). Magneto-induced splittings of P' peaks in 3R-WSe₂ are indicated in (b) by dashed lines. (c) and (d) Valley Zeeman splitting Δ of all peaks identified in 2H- and 3R-WSe₂ magnetoluminescence as a function of magnetic field. The respective exciton g factors were extracted from linear fits (solid lines) to the data and grouped by colors. (e) and (f) Schematic illustration of momentum-direct and phonon-assisted transitions in 2H and 3R, tagged with theoretical exciton g -factor values (solid and dashed lines denote spin-up and spin-down bands; orange and red colors indicate the bands of the first and second layers degenerate in 2H but split in 3R stacking).

resolved magnetoluminescence spectra of 2H- and 3R-WSe₂ BLs, recorded at $B = -8$ T with σ^+ and σ^- circular detection under linearly polarized (π) excitation, are shown in Figs. 4(a) and 4(b). The exciton g factors follow from linear fits to the data shown by solid lines in Figs. 4(c) and 4(d) and grouped in color according to the g -factor values.

For 2H [Fig. 4(c)], we found for the fundamental exciton peak X the characteristic g factor of -4.3 as well as g factors of momentum-indirect QK excitons (i.e., Coulomb-correlated states of the conduction band electron in the Q valley and the valence band vacancy in the K valley) in the range from -9.3 to -10.9 (peaks P_1 – P_4), consistent with previous findings for exfoliated WSe₂ BLs in 2H stacking [28]. In 3R stacking, our high-quality sample with spectrally narrow PL emission allows us to quantify two distinct g factors of -4.3 and -4.8 for the momentum-direct KK exciton doublet X_1 and X_2 [Fig. 4(d)]. For the emission peaks at lower energy between 1.50 and 1.55 eV, we determined g factors of ~ -11 as in 2H (peaks P_1 – P_4) and an additional group of peaks (peaks P'_1 – P'_3) with a g factor ~ -14 . According to our understanding of the band structure and exciton g factors in 2H-WSe₂ BL, the peaks P_1 – P_4 stem from phonon-assisted recombination of QK excitons, without contribution of $Q\Gamma$ states with small g factors between 0 and 4 [28].

To interpret the origin of additional peaks in 3R stacking with distinct magnetoluminescence features as well as their difference from the 2H configuration, we calculated the exciton g factors from first principles [28,68,73–75]. The results for both stackings are presented in Table I and pictorially in Figs. 4(e) and 4(f). In the case of 2H, the g factor of X corresponds to spinlike ($\uparrow\uparrow$) KK transition, whereas momentum-indirect exciton peaks (P_1 – P_4) relate to spinlike intralayer QK and interlayer $Q'K$ transitions with $g = -9.51$. For transitions in 3R, our results also identify spinlike KK excitons X_1 and X_2 with two different g factors of -4.18 and -3.63 . This difference in the theoretical values arises from different g factors of the conduction bands at K in the top and bottom layers L_1 and L_2 .

Momentum-indirect excitons with peaks P_1 – P_4 in 3R with similar g factors to the corresponding peaks in 2H stem from spinlike intralayer and interlayer QK transitions with $g = -8.86$ and -9.78 , respectively. Additional 3R peaks with relatively large g factors (P'_1 – P'_3), on the other hand, originate from spin-unlike intralayer and interlayer $Q'K$ transitions with g factors of -13.80 and -13.76 . We note that, in 2H, spin-unlike intralayer $Q'K$ and interlayer QK transitions with $g = -13.71$ from Table I are not observed within the signal-to-noise ratio of our experiment. These states are degenerate

TABLE I. Theoretical exciton g factors in $2H$ - and $3R$ -WSe₂ bilayers. We distinguish between intra- and interlayer excitons and show for momentum-direct KK transitions only the g factors of intralayer excitons. For momentum-indirect QK and $Q'K$ transitions, we select spin-valley configurations of intra- and interlayer excitons with the lowest energies. The transition column ($L_{cb} \rightarrow L_{vb}$) indicates the layers with conduction and valence band electrons involved in phonon-assisted recombination.

Exciton			Transition	g factors	
Intra	Inter	Spin		$2H$	$3R$
KK		$\uparrow\uparrow$	$L_1 \rightarrow L_1$	-4.04	-3.63
KK		$\uparrow\uparrow$	$L_2 \rightarrow L_2$		-4.18
QK		$\uparrow\uparrow$	$L_1 \rightarrow L_1$	-9.51	-8.86
	QK	$\uparrow\uparrow$	$L_1 \rightarrow L_2$		-9.78
	$Q'K$	$\uparrow\uparrow$	$L_1 \rightarrow L_2$	-9.51	
$Q'K$		$\downarrow\uparrow$	$L_1 \rightarrow L_1$	-13.71	-13.76
	$Q'K$	$\downarrow\uparrow$	$L_1 \rightarrow L_2$		-13.80
	QK	$\downarrow\uparrow$	$L_1 \rightarrow L_2$	-13.71	

with the two respective spinlike interlayer $Q'K$ and intralayer QK transitions, yet their exciton population seems to be vanishingly small, presumably due to spin-conserving relaxation [10]. However, once the degeneracy of the states is removed by the lack of inversion symmetry in $3R$ stacking, our analysis shows that spin-unlike $Q'K$ excitons light up in the PL of peaks P'_1 - P'_3 .

III. CONCLUSIONS

Our extensive experimental and theoretical studies of BL WSe₂ identify stacking-dependent optical response of $2H$ and $3R$ crystals. We find the marked differences to arise from distinct multiplicity of intralayer and interlayer excitons in the two different stable realizations of BL stackings. Using high-quality samples of both stacking configurations by CVD crystal synthesis and hBN encapsulation, we obtain spectrally narrow resonances which allow us to identify in great detail the characteristics of momentum-direct excitons in absorption and momentum-indirect excitons in emission of $2H$ and $3R$ BLs. For both stackings, we find that the lowest-energy PL is dominated by momentum-indirect QK and $Q'K$ excitons with intralayer and interlayer characters. The different degrees of layer delocalization give rise to two different electrostatic dipoles, providing an explanation for the recent observations of two distinct slopes in the first-order Stark effect [20,21]. Moreover, our results demonstrate that exciton state multiplicity, transition energies, and oscillator strengths sensitively depend on the BL stacking order and highlight how layer-degenerate excitons in inversion symmetric $2H$ BLs split into exciton doublets in $3R$ stacking with broken inversion symmetry and different atomic registries for the top and bottom layers. Our findings are relevant for the understanding of other TMD homobilayer systems as well as semiconductor van der Waals heterobilayers with varying degrees of symmetry, twist, and interlayer hybridization.

IV. METHODS

A. Synthesis of homobilayer WSe₂

Homobilayer WSe₂ crystals were synthesized on thermally oxidized silicon substrates (with a SiO₂ thickness of 285 nm) using WO₂ and Se powders (99.99%, Sigma-Aldrich) as precursors and the vapor phase chalcogenization method to obtain high-quality crystalline samples [76,77] with addition of NaCl [78] for higher yield. A three-zone furnace CVD system (Carbolite Gero) equipped with a 1-inch quartz tube was used for the growth. An alumina boat containing mixed powder of WO₂ (40 mg) and NaCl (5 mg) was placed at the center of the first zone, and a SiO₂/Si substrate was located face-down above the WO₂ powder. Another crucible boat containing Se was placed 25 cm upstream from the center of the first zone. After the tube was evacuated to ~ 10 mTorr several times to remove air and moisture, the reaction chamber pressure was increased to ambient pressure through 500 sccm argon gas flow. Then the furnace was heated with a ramping rate of 50 °C/min to the target growth temperature and kept there for 5 min with 140/10 sccm Ar/H₂ gas flow before cooling down. In general, the yield of $3R$ stacked crystals was highest at 960 °C, while $2H$ stacking was obtained at higher temperatures.

B. Sample fabrication

A Polydimethylsiloxane/Polycarbonate (PDMS/PC) stamp was used to sequentially pick up the exfoliated hBN layers (NIMS) and CVD-grown homobilayer WSe₂ crystals using the dry transfer method [79,80]. Poly-(bisphenol A-carbonate) pellets (Sigma Aldrich) were dissolved in chloroform with a weight ratio of 8. The mixture was stirred at 500 rpm using a magneton bar at room temperature overnight. The well-dissolved PC film was mounted on a PDMS block on a glass slide. First, the top hBN layer with a thickness of 163 nm for $2H$ (161 nm for $3R$) was picked up with the stamp, followed by $2H$ - or $3R$ -WSe₂ BL and the bottom hBN layer with a thickness of 67 nm for $2H$ (66 nm for $3R$). The pick-up temperatures for the hBN flakes and WSe₂ BLs were ~ 50 °C and 140 °C, respectively. The entire stack was released at a temperature of 180 °C onto a Si/SiO₂ target substrate, then soaked in chloroform solution for 20 min to remove PC residues, cleaned by acetone and isopropanol, and annealed at 200 °C under ultrahigh vacuum for 15 h.

C. Optical spectroscopy

Raman spectra were recorded at room temperature under ambient conditions using a Raman system (T64000, Horiba) with 40 μ W laser excitation at 532 nm and a spectral resolution of 0.3 cm⁻¹ with a 2400 grooves/mm grating. Low-temperature PL and DR measurements were performed with a microspectroscopy setup assembled around a closed-cycle magnetocryostat (attocube systems, attoDRY1000) equipped with nanopositioners (attocube systems, ANP101 series), a low-temperature apochromatic micro-objective (attocube systems, LT-APO/VISIR/0.82), and a bidirectional solenoid for magnetic fields of up to 9 T in Faraday configuration. A halogen lamp (HL 2000, Ocean Optics) or pulsed supercontinuum laser (NKT, SuperK Extreme) was used for reflectivity

measurements. Differential reflectivity spectra were obtained by normalizing the reflected light intensity from the hBN encapsulated homobilayer region to that from a bare hBN region. For PL measurements, the sample was excited at powers ranging from 10 to 50 μW either by a continuous-wave laser diode at 670 nm or pulsed supercontinuum laser with a 10 nm bandwidth ~ 670 nm. The spectra were detected with a charge-coupled device cooled by liquid nitrogen (Roper Scientific, Spec 10:100BR/LN) dispersed with a monochromator (Roper Scientific, Acton SP2500).

D. Theoretical calculations

The atomic structures, the quasiparticle band structures, and optical spectra have been obtained using the VASP package [81,82]. Core electrons have been treated by the plane-augmented wave scheme [83,84]. A lattice parameter value of 3.32 Å has been set for all calculation runs. A grid of $15 \times 15 \times 1$ k-points has been used, in conjunction with a vacuum height of 21.9 Å, for all the calculation cells. The optimization process of the geometry has been performed at the PBE-D3 level [85] to include van der Waals interaction between layers. All the atoms were allowed to relax with a force convergence criterion < 0.005 eV/Å. The Heyd-Scuseria-Ernzerhof hybrid functional [86–88] has been used as an approximation of the exchange-correlation electronic term, including SOC, to determine eigenvalues and wave functions as input for g -factor calculations and the full-frequency-dependent GW calculations [89] performed at the G_0W_0 level. An energy cutoff of 400 eV and a Gaussian smearing of 0.05 eV width have been chosen for partial occupancies, when a tight electronic minimization tolerance of 10^{-8} eV was set to determine with good precision the corresponding derivative of the orbitals with respect to k needed in quasiparticle band structure calculations. The total number of states included in the GW procedure is set to 1280, in conjunction with an energy cutoff of 100 eV for the response function, after a careful check of the direct bandgap

convergence (< 0.1 eV as a function of k-points sampling). Band structures have been obtained after a Wannier interpolation procedure performed by the WANNIER90 program [84]. All optical excitonic transitions have been calculated by solving the BSE [90,91], using the 12 highest valence bands and the 16 lowest conduction bands to obtain eigenvalues and oscillator strengths on all systems. From these calculations, we report the absorbance values by using the imaginary part of the complex dielectric function constructed with a broadening of 12 meV.

Note added. During the preparation of our manuscript, we became aware of a related work on stacking-dependent optical properties in BL WSe_2 [92].

ACKNOWLEDGMENTS

We thank P. Altpeter and C. Obermayer for assistance in the clean room and the group of T. Weitz for providing access to their Raman spectrometer. This paper was funded by the European Research Council under Grant Agreement No. 772195 as well as the Deutsche Forschungsgemeinschaft within the Priority Programme SPP 2244 2DMP (Project No. 443405595) and Germany's Excellence Strategy Munich Center for Quantum Science and Technology (EXC-2111-390814868). Z.L. acknowledges funding by the China Scholarship Council through Grant No. 201808140196. I.B. gratefully acknowledges financial support from the Alexander von Humboldt Foundation. A.H. acknowledges support from the Center for NanoScience and the LMUinnovativ project Functional Nanosystems. B.U. acknowledges funding from ANR IXTASE. I.C.G. thanks the CALMIP initiative for the generous allocation of computational time, through Project No. p0812, as well as GENCI-CINES and GENCI-IDRIS for Grant No. A010096649. K.W. and T.T. acknowledge support from JSPS KAKENHI (Grants No. 19H05790, No. 20H00354, and No. 21H05233).

-
- [1] G. Wang, A. Chernikov, M. M. Glazov, T. F. Heinz, X. Marie, T. Amand, and B. Urbaszek, Colloquium: Excitons in atomically thin transition metal dichalcogenides, *Rev. Mod. Phys.* **90**, 021001 (2018).
- [2] N. P. Wilson, W. Yao, J. Shan, and X. Xu, Excitons and emergent quantum phenomena in stacked 2D semiconductors, *Nature (London)* **599**, 383 (2021).
- [3] W. Zhao, R. M. Ribeiro, M. Toh, A. Carvalho, C. Kloc, A. H. Castro Neto, and G. Eda, Origin of indirect optical transitions in few-layer MoS_2 , WS_2 , and WSe_2 , *Nano Lett.* **13**, 5627 (2013).
- [4] A. Arora, M. Drüppel, R. Schmidt, T. Deilmann, R. Schneider, M. R. Molas, P. Marauhn, S. M. de Vasconcellos, M. Potemski, M. Rohlfiing *et al.*, Interlayer excitons in a bulk van der Waals semiconductor, *Nat. Commun.* **8**, 639 (2017).
- [5] M. R. Molas, K. Nogajewski, A. O. Slobodeniuk, J. Binder, M. Bartos, and M. Potemski, The optical response of monolayer, few-layer and bulk tungsten disulfide, *Nanoscale* **9**, 13128 (2017).
- [6] L. Wang, E.-M. Shih, A. Ghiotto, L. Xian, D. A. Rhodes, C. Tan, M. Claassen, D. M. Kennes, Y. Bai, B. Kim *et al.*, Correlated electronic phases in twisted bilayer transition metal dichalcogenides, *Nat. Mater.* **19**, 861 (2020).
- [7] S. Brem, K.-Q. Lin, R. Gillen, J. M. Bauer, J. Maultzsch, J. M. Lupton, and E. Malic, Hybridized intervalley moiré excitons and flat bands in twisted WSe_2 bilayers, *Nanoscale* **12**, 11088 (2020).
- [8] T. I. Andersen, G. Scuri, A. Sushko, K. De Greve, J. Sung, Y. Zhou, D. S. Wild, R. J. Gelly, H. Heo, D. Bérubé *et al.*, Excitons in a reconstructed moiré potential in twisted $\text{WSe}_2/\text{WSe}_2$ homobilayers, *Nat. Mater.* **20**, 480 (2021).
- [9] Z. Gong, G.-B. Liu, H. Yu, D. Xiao, X. Cui, X. Xu, and W. Yao, Magnetoelectric effects and valley-controlled spin quantum gates in transition metal dichalcogenide bilayers, *Nat. Commun.* **4**, 2053 (2013).
- [10] G. Scuri, T. I. Andersen, Y. Zhou, D. S. Wild, J. Sung, R. J. Gelly, D. Bérubé, H. Heo, L. Shao, A. Y. Joe *et al.*, Electrically Tunable Valley Dynamics in Twisted $\text{WSe}_2/\text{WSe}_2$ Bilayers, *Phys. Rev. Lett.* **124**, 217403 (2020).
- [11] P. Merkl, F. Mooshammer, S. Brem, A. Girnghuber, K.-Q. Lin, L. Weigl, M. Liebich, C.-K. Yong, R. Gillen, J. Maultzsch

- et al.*, Twist-tailoring Coulomb correlations in van der Waals homobilayers, *Nat. Commun.* **11**, 2167 (2020).
- [12] K.-Q. Lin, P. E. Faria Junior, J. M. Bauer, B. Peng, B. Monserrat, M. Gmitra, J. Fabian, S. Bange, and J. M. Lupton, Twist-angle engineering of excitonic quantum interference and optical nonlinearities in stacked 2D semiconductors, *Nat. Commun.* **12**, 1553 (2021).
- [13] E. V. Calman, M. M. Fogler, L. V. Butov, S. Hu, A. Mishchenko, and A. K. Geim, Indirect excitons in van der Waals heterostructures at room temperature, *Nat. Commun.* **9**, 1895 (2018).
- [14] T. Deilmann and K. S. Thygesen, Interlayer excitons with large optical amplitudes in layered van der Waals materials, *Nano Lett.* **18**, 2984 (2018).
- [15] I. C. Gerber, E. Courtade, S. Shree, C. Robert, T. Taniguchi, K. Watanabe, A. Balocchi, P. Renucci, D. Lagarde, X. Marie *et al.*, Interlayer excitons in bilayer MoS₂ with strong oscillator strength up to room temperature, *Phys. Rev. B* **99**, 035443 (2019).
- [16] Z. Wang, Y.-H. Chiu, K. Honz, K. F. Mak, and J. Shan, Electrical tuning of interlayer exciton gases in WSe₂ bilayers, *Nano Lett.* **18**, 137 (2018).
- [17] N. Leisgang, S. Shree, I. Paradisanos, L. Sponfeldner, C. Robert, D. Lagarde, A. Balocchi, K. Watanabe, T. Taniguchi, X. Marie *et al.*, Giant Stark splitting of an exciton in bilayer MoS₂, *Nat. Nanotechnol.* **15**, 901 (2020).
- [18] N. Peimiyoo, T. Deilmann, F. Withers, J. Escolar, D. Nutting, T. Taniguchi, K. Watanabe, A. Taghizadeh, M. F. Craciun, K. S. Thygesen *et al.*, Electrical tuning of optically active interlayer excitons in bilayer MoS₂, *Nat. Nanotechnol.* **16**, 888 (2021).
- [19] E. Lorchat, M. Selig, F. Katsch, K. Yumigeta, S. Tongay, A. Knorr, C. Schneider, and S. Höfling, Excitons in Bilayer MoS₂ Displaying a Colossal Electric Field Splitting and Tunable Magnetic Response, *Phys. Rev. Lett.* **126**, 037401 (2021).
- [20] M. M. Altairy, E. Liu, C.-T. Liang, F.-C. Hsiao, J. van Baren, T. Taniguchi, K. Watanabe, N. M. Gabor, Y.-C. Chang, and C. H. Lui, Electric-field-tunable intervalley excitons and phonon replicas in bilayer WSe₂, *Nano Lett.* **22**, 1829 (2022).
- [21] Z. Huang, Y. Zhao, T. Bo, Y. Chu, J. Tian, L. Liu, Y. Yuan, F. Wu, J. Zhao, L. Xian *et al.*, Spatially indirect intervalley excitons in bilayer WSe₂, *Phys. Rev. B* **105**, L041409 (2022).
- [22] L. Yuanda, D. Kévin, T. Qinghai, L. Timothy, S. Novoselov Kostya, and G. Weibo, Electrically controllable router of interlayer excitons, *Sci. Adv.* **6**, eaba1830 (2021).
- [23] W.-T. Hsu, B.-H. Lin, L.-S. Lu, M.-H. Lee, M.-W. Chu, L.-J. Li, W. Yao, W.-H. Chang, and C.-K. Shih, Tailoring excitonic states of van der Waals bilayers through stacking configuration, band alignment, and valley spin, *Sci. Adv.* **5**, eaax7407 (2019).
- [24] I. Paradisanos, S. Shree, A. George, N. Leisgang, C. Robert, K. Watanabe, T. Taniguchi, R. J. Warburton, A. Turchanin, X. Marie *et al.*, Controlling interlayer excitons in MoS₂ layers grown by chemical vapor deposition, *Nat. Commun.* **11**, 2391 (2020).
- [25] K. F. Mak, C. Lee, J. Hone, J. Shan, and T. F. Heinz, Atomically Thin MoS₂: A New Direct-Gap Semiconductor, *Phys. Rev. Lett.* **105**, 136805 (2010).
- [26] A. Splendiani, L. Sun, Y. Zhang, T. Li, J. Kim, C.-Y. Chim, G. Galli, and F. Wang, Emerging photoluminescence in monolayer MoS₂, *Nano Lett.* **10**, 1271 (2010).
- [27] J. Lindlau, M. Selig, A. Neumann, L. Colombier, J. Förste, V. Funk, M. Förg, J. Kim, G. Berghäuser, T. Taniguchi *et al.*, The role of momentum-dark excitons in the elementary optical response of bilayer WSe₂, *Nat. Commun.* **9**, 2586 (2018).
- [28] J. Förste, N. V. Tepliakov, S. Yu. Kruchinin, J. Lindlau, V. Funk, M. Förg, K. Watanabe, T. Taniguchi, A. S. Baimuratov, and A. Högele, Exciton *g*-factors in monolayer and bilayer WSe₂ from experiment and theory, *Nat. Commun.* **11**, 4539 (2020).
- [29] V. Funk, K. Wagner, E. Wietek, J. D. Ziegler, J. Förste, J. Lindlau, M. Förg, K. Watanabe, T. Taniguchi, A. Chernikov *et al.*, Spectral asymmetry of phonon sideband luminescence in monolayer and bilayer WSe₂, *Phys. Rev. Research* **3**, L042019 (2021).
- [30] O. B. Aslan, M. Deng, M. L. Brongersma, and T. F. Heinz, Strained bilayer WSe₂ with reduced exciton-phonon coupling, *Phys. Rev. B* **101**, 115305 (2020).
- [31] K. Liu, L. Zhang, T. Cao, C. Jin, D. Qiu, Q. Zhou, A. Zettl, P. Yang, S. G. Louie, and F. Wang, Evolution of interlayer coupling in twisted molybdenum disulfide bilayers, *Nat. Commun.* **5**, 4966 (2014).
- [32] L. M. Schneider, J. Kuhnert, S. Schmitt, W. Heimbrod, U. Huttner, L. Meckbach, T. Stroucken, S. W. Koch, S. Fu, X. Wang *et al.*, Spin-layer and spin-valley locking in CVD-grown AA'- and AB-stacked tungsten-disulfide bilayers, *J. Phys. Chem. C* **123**, 21813 (2019).
- [33] L. Du, Q. Zhang, T. Zhang, Z. Jia, J. Liang, G.-B. Liu, R. Yang, D. Shi, J. Xiang, K. Liu *et al.*, Robust circular polarization of indirect Q-K transitions in bilayer 3R-WS₂, *Phys. Rev. B* **100**, 161404(R) (2019).
- [34] S. Carr, D. Massatt, S. B. Torrisi, P. Cazeaux, M. Lusk, and E. Kaxiras, Relaxation and domain formation in incommensurate two-dimensional heterostructures, *Phys. Rev. B* **98**, 224102 (2018).
- [35] A. Weston, Y. Zou, V. Enaldiev, A. Summerfield, N. Clark, V. Zólyomi, A. Graham, C. Yelgel, S. Magorrian, M. Zhou *et al.*, Atomic reconstruction in twisted bilayers of transition metal dichalcogenides, *Nat. Nanotechnol.* **15**, 592 (2020).
- [36] V. V. Enaldiev, V. Zólyomi, C. Yelgel, S. J. Magorrian, and V. I. Fal'ko, Stacking Domains and Dislocation Networks in Marginally Twisted Bilayers of Transition Metal Dichalcogenides, *Phys. Rev. Lett.* **124**, 206101 (2020).
- [37] S. J. Magorrian, V. V. Enaldiev, V. Zólyomi, F. Ferreira, V. I. Fal'ko, and D. A. Ruiz-Tijerina, Multifaceted moiré superlattice physics in twisted WSe₂ bilayers, *Phys. Rev. B* **104**, 125440 (2021).
- [38] Y. Kenji, W. Xirui, W. Kenji, T. Takashi, and J.-H. Pablo, Stacking-engineered ferroelectricity in bilayer boron nitride, *Science* **372**, 1458 (2021).
- [39] M. Vizner Stern, Y. Waschitz, W. Cao, I. Nevo, K. Watanabe, T. Taniguchi, E. Sela, M. Urbakh, O. Hod, and M. Ben Shalom, Interfacial ferroelectricity by van der Waals sliding, *Science* **372**, 1462 (2021).
- [40] C. Woods, P. Ares, H. Nevison-Andrews, M. Holwill, R. Fabregas, F. Guinea, A. Geim, K. Novoselov, N. Walet, and L. Fumagalli, Charge-polarized interfacial superlattices in marginally twisted hexagonal boron nitride, *Nat. Commun.* **12**, 347 (2021).
- [41] F. Ferreira, V. V. Enaldiev, V. I. Fal'ko, and S. J. Magorrian, Weak ferroelectric charge transfer in layer-asymmetric bilayers of 2D semiconductors, *Sci. Rep.* **11**, 13422 (2021).

- [42] A. Weston, E. G. Castanon, V. Enaldiev, F. Ferreira, S. Bhattacharjee, S. Xu, H. Corte-Leon, Z. Wu, N. Clark, A. Summerfield *et al.*, Interfacial ferroelectricity in marginally twisted 2D semiconductors, *Nat. Nanotechnol.* **17**, 390 (2022).
- [43] H. Li, G. Lu, Y. Wang, Z. Yin, C. Cong, Q. He, L. Wang, F. Ding, T. Yu, and H. Zhang, Mechanical exfoliation and characterization of single- and few-layer nanosheets of WSe₂, TaS₂, and TaSe₂, *Small* **9**, 1974 (2013).
- [44] H. Zeng, G.-B. Liu, J. Dai, Y. Yan, B. Zhu, R. He, L. Xie, S. Xu, X. Chen, W. Yao *et al.*, Optical signature of symmetry variations and spin-valley coupling in atomically thin tungsten dichalcogenides, *Sci. Rep.* **3**, 1608 (2013).
- [45] H. Sahin, S. Tongay, S. Horzum, W. Fan, J. Zhou, J. Li, J. Wu, and F. M. Peeters, Anomalous Raman spectra and thickness-dependent electronic properties of WSe₂, *Phys. Rev. B* **87**, 165409 (2013).
- [46] W. Zhao, Z. Ghorannevis, K. K. Amara, J. R. Pang, M. Toh, X. Zhang, C. Kloc, P. H. Tan, and G. Eda, Lattice dynamics in mono- and few-layer sheets of WS₂ and WSe₂, *Nanoscale* **5**, 9677 (2013).
- [47] X. Luo, Y. Zhao, J. Zhang, M. Toh, C. Kloc, Q. Xiong, and S. Y. Quek, Effects of lower symmetry and dimensionality on Raman spectra in two-dimensional WSe₂, *Phys. Rev. B* **88**, 195313 (2013).
- [48] H. Terrones, E. D. Corro, S. Feng, J. M. Poumirol, D. Rhodes, D. Smirnov, N. R. Pradhan, Z. Lin, M. A. T. Nguyen, A. L. Elías *et al.*, New first order Raman-active modes in few layered transition metal dichalcogenides, *Sci. Rep.* **4**, 4215 (2014).
- [49] A. A. Puretzky, L. Liang, X. Li, K. Xiao, K. Wang, M. Mahjouri-Samani, L. Basile, J. C. Idrobo, B. G. Sumpter, V. Meunier *et al.*, Low-frequency Raman fingerprints of two-dimensional metal dichalcogenide layer stacking configurations, *ACS Nano* **9**, 6333 (2015).
- [50] F. Cadiz, E. Courtade, C. Robert, G. Wang, Y. Shen, H. Cai, T. Taniguchi, K. Watanabe, H. Carrere, D. Lagarde *et al.*, Excitonic Linewidth Approaching the Homogeneous Limit in MoS₂-Based van der Waals Heterostructures, *Phys. Rev. X* **7**, 021026 (2017).
- [51] O. A. Ajayi, J. V. Ardelean, G. D. Shepard, J. Wang, A. Antony, T. Taniguchi, K. Watanabe, T. F. Heinz, S. Strauf, X.-Y. Zhu *et al.*, Approaching the intrinsic photoluminescence linewidth in transition metal dichalcogenide monolayers, *2D Mater.* **4**, 031011 (2017).
- [52] J. Wierzbowski, J. Klein, F. Sigger, C. Straubinger, M. Kremser, T. Taniguchi, K. Watanabe, U. Wurstbauer, A. W. Holleitner, M. Kaniber *et al.*, Direct exciton emission from atomically thin transition metal dichalcogenide heterostructures near the lifetime limit, *Sci. Rep.* **7**, 12383 (2017).
- [53] S. Shree, A. George, T. Lehnert, C. Neumann, M. Benelajla, C. Robert, X. Marie, K. Watanabe, T. Taniguchi, U. Kaiser *et al.*, High optical quality of MoS₂ monolayers grown by chemical vapor deposition, *2D Mater.* **7**, 015011 (2019).
- [54] Y. You, X.-X. Zhang, T. C. Berkelbach, M. S. Hybertsen, D. R. Reichman, and T. F. Heinz, Observation of biexcitons in monolayer WSe₂, *Nat. Phys.* **11**, 477 (2015).
- [55] M. Barbone, A. R.-P. Montblanch, D. M. Kara, C. Palacios-Berraquero, A. R. Cadore, D. De Fazio, B. Pingault, E. Mostaani, H. Li, B. Chen *et al.*, Charge-tunable biexciton complexes in monolayer WSe₂, *Nat. Commun.* **9**, 3721 (2018).
- [56] A. Steinhoff, M. Florian, A. Singh, K. Tran, M. Kolarczik, S. Helmrich, A. W. Achtstein, U. Woggon, N. Owschimikow, F. Jahnke *et al.*, Biexciton fine structure in monolayer transition metal dichalcogenides, *Nat. Phys.* **14**, 1199 (2018).
- [57] Z. Li, T. Wang, Z. Lu, C. Jin, Y. Chen, Y. Meng, Z. Lian, T. Taniguchi, K. Watanabe, S. Zhang *et al.*, Revealing the biexciton and trion-exciton complexes in BN encapsulated WSe₂, *Nat. Commun.* **9**, 3719 (2018).
- [58] Z. Ye, L. Waldecker, E. Y. Ma, D. Rhodes, A. Antony, B. Kim, X.-X. Zhang, M. Deng, Y. Jiang, Z. Lu *et al.*, Efficient generation of neutral and charged biexcitons in encapsulated WSe₂ monolayers, *Nat. Commun.* **9**, 3718 (2018).
- [59] A. Arora, M. Koperski, K. Nogajewski, J. Marcus, C. Faugeras, and M. Potemski, Excitonic resonances in thin films of WSe₂: From monolayer to bulk material, *Nanoscale* **7**, 10421 (2015).
- [60] D. Wickramaratne, F. Zahid, and R. K. Lake, Electronic and thermoelectric properties of few-layer transition metal dichalcogenides, *J. Chem. Phys.* **140**, 124710 (2014).
- [61] J. Sung, Y. Zhou, G. Scuri, V. Zólyomi, T. I. Andersen, H. Yoo, D. S. Wild, A. Y. Joe, R. J. Gelly, H. Heo *et al.*, Broken mirror symmetry in excitonic response of reconstructed domains in twisted MoSe₂/MoSe₂ bilayers, *Nat. Nanotechnol.* **15**, 750 (2020).
- [62] I. C. Gerber and X. Marie, Dependence of band structure and exciton properties of encapsulated WSe₂ monolayers on the hBN-layer thickness, *Phys. Rev. B* **98**, 245126 (2018).
- [63] A. O. Slobodeniuk, M. Koperski, M. R. Molas, P. Kossacki, K. Nogajewski, M. Bartos, K. Watanabe, T. Taniguchi, C. Faugeras, and M. Potemski, Fine structure of K-excitons in multilayers of transition metal dichalcogenides, *2D Mater.* **6**, 025026 (2019).
- [64] J. Horng, T. Stroucken, L. Zhang, E. Y. Paik, H. Deng, and S. W. Koch, Observation of interlayer excitons in MoSe₂ single crystals, *Phys. Rev. B* **97**, 241404(R) (2018).
- [65] A. Arora, T. Deilmann, P. Marauhn, M. Drüppel, R. Schneider, M. R. Molas, D. Vaclavkova, S. M. de Vasconcellos, M. Rohlfing, M. Potemski *et al.*, Valley-contrasting optics of interlayer excitons in Mo- and W-based bulk transition metal dichalcogenides, *Nanoscale* **10**, 15571 (2018).
- [66] D. Yang, J. Wu, B. T. Zhou, J. Liang, T. Ideue, T. Siu, K. M. Awan, K. Watanabe, T. Taniguchi, Y. Iwasa *et al.*, Spontaneous-polarization-induced photovoltaic effect in rhombohedrally stacked MoS₂, *Nat. Photonics* **16**, 469 (2022).
- [67] S. Shree, I. Paradisanos, X. Marie, C. Robert, and B. Urbaszek, Guide to optical spectroscopy of layered semiconductors, *Nat. Rev. Phys.* **3**, 39 (2021).
- [68] M. Förg, A. S. Baimuratov, S. Yu. Kruchinin, I. A. Vovk, J. Scherzer, and A. Högele, Moiré excitons in MoSe₂ – WSe₂ heterobilayers and heterotrilayers, *Nat. Commun.* **12**, 1656 (2021).
- [69] G. Aivazian, Z. Gong, A. M. Jones, R.-L. Chu, J. Yan, D. G. Mandrus, C. Zhang, D. Cobden, W. Yao, and X. Xu, Magnetic control of valley pseudospin in monolayer WSe₂, *Nat. Phys.* **11**, 148 (2015).
- [70] A. Srivastava, M. Sidler, A. V. Allain, D. S. Lembke, A. Kis, and A. Imamoglu, Valley Zeeman effect in elementary optical excitations of monolayer WSe₂, *Nat. Phys.* **11**, 141 (2015).
- [71] G. Wang, L. Bouet, M. M. Glazov, T. Amand, E. L. Ivchenko, E. Palleau, X. Marie, and B. Urbaszek, Magneto-optics in

- transition metal diselenide monolayers, *2D Mater.* **2**, 034002 (2015).
- [72] M. Koperski, M. R. Molas, A. Arora, K. Nogajewski, M. Bartos, J. Wyzula, D. Vaclavkova, P. Kossacki, and M. Potemski, Orbital, spin and valley contributions to Zeeman splitting of excitonic resonances in MoSe₂, WSe₂ and WS₂ Monolayers, *2D Mater.* **6**, 015001 (2018).
- [73] T. Wozniak, P. E. Faria Junior, G. Seifert, A. Chaves, and J. Kunstmann, Exciton *g* factors of van der Waals heterostructures from first-principles calculations, *Phys. Rev. B* **101**, 235408 (2020).
- [74] T. Deilmann, P. Krüger, and M. Rohlfing, *Ab Initio* Studies of Exciton *g* Factors: Monolayer Transition Metal Dichalcogenides in Magnetic Fields, *Phys. Rev. Lett.* **124**, 226402 (2020).
- [75] F. Xuan and S. Y. Quek, Valley Zeeman effect and Landau levels in two-dimensional transition metal dichalcogenides, *Phys. Rev. Research* **2**, 033256 (2020).
- [76] I. Bilgin, F. Liu, A. Vargas, A. Winchester, M. K. L. Man, M. Upmanyu, K. M. Dani, G. Gupta, S. Talapatra, A. D. Mohite *et al.*, Chemical vapor deposition synthesized atomically thin molybdenum disulfide with optoelectronic-grade crystalline quality, *ACS Nano* **9**, 8822 (2015).
- [77] I. Bilgin, A. S. Raeliarijaona, M. C. Lucking, S. C. Hodge, A. D. Mohite, A. de Luna Bugallo, H. Terrones, and S. Kar, Resonant Raman and exciton coupling in high-quality single crystals of atomically thin molybdenum diselenide grown by vapor-phase chalcogenization, *ACS Nano* **12**, 740 (2018).
- [78] S. Li, S. Wang, D.-M. Tang, W. Zhao, H. Xu, L. Chu, Y. Bando, D. Golberg, and G. Eda, Halide-assisted atmospheric pressure growth of large WSe₂ and WS₂ monolayer crystals, *Appl. Mater. Today* **1**, 60 (2015).
- [79] F. Pizzocchero, L. Gammelgaard, B. S. Jessen, J. M. Caridad, L. Wang, J. Hone, P. Bøggild, and T. J. Booth, The hot pick-up technique for batch assembly of van der Waals heterostructures, *Nat. Commun.* **7**, 11894 (2016).
- [80] D. G. Purdie, N. M. Pugno, T. Taniguchi, K. Watanabe, A. C. Ferrari, and A. Lombardo, Cleaning interfaces in layered materials heterostructures, *Nat. Commun.* **9**, 5387 (2018).
- [81] G. Kresse and J. Hafner, *Ab initio* molecular-dynamics simulation of the liquid-metal–amorphous-semiconductor transition in germanium, *Phys. Rev. B* **49**, 14251 (1994).
- [82] G. Kresse and J. Furthmüller, Efficient iterative schemes for *ab initio* total-energy calculations using a plane-wave basis set, *Phys. Rev. B* **54**, 11169 (1996).
- [83] P. E. Blöchl, Projector augmented-wave method, *Phys. Rev. B* **50**, 17953 (1994).
- [84] A. A. Mostofi, J. R. Yates, Y.-S. Lee, I. Souza, D. Vanderbilt, and N. Marzari, WANNIER90: A tool for obtaining maximally-localised Wannier functions, *Comput. Phys. Commun.* **178**, 685 (2008).
- [85] S. Grimme, J. Antony, S. Ehrlich, and H. Krieg, A consistent and accurate *ab initio* parametrization of density functional dispersion correction (DFT-D) for the 94 elements H-Pu, *J. Chem. Phys.* **132**, 154104 (2010).
- [86] J. Heyd and G. E. Scuseria, Assessment and validation of a screened Coulomb hybrid density functional, *J. Chem. Phys.* **120**, 7274 (2004).
- [87] J. Heyd, J. E. Peralta, G. E. Scuseria, and R. L. Martin, Energy band gaps and lattice parameters evaluated with the Heyd-Scuseria-Ernzerhof screened hybrid functional, *J. Chem. Phys.* **123**, 174101 (2005).
- [88] J. Paier, M. Marsman, K. Hummer, G. Kresse, I. C. Gerber, and J. G. Ángyán, Screened hybrid density functionals applied to solids, *J. Chem. Phys.* **124**, 154709 (2006).
- [89] M. Shishkin and G. Kresse, Implementation and performance of the frequency-dependent *GW* method within the PAW framework, *Phys. Rev. B* **74**, 035101 (2006).
- [90] W. Hanke and L. J. Sham, Many-Particle Effects in the Optical Excitations of a Semiconductor, *Phys. Rev. Lett.* **43**, 387 (1979).
- [91] M. Rohlfing and S. G. Louie, Electron-Hole Excitations in Semiconductors and Insulators, *Phys. Rev. Lett.* **81**, 2312 (1998).
- [92] K. M. McCreary, M. Phillips, H.-J. Chuang, D. Wickramaratne, M. Rosenberger, C. S. Hellberg, and B. T. Jonker, Stacking-dependent optical properties in bilayer WSe₂, *Nanoscale* **14**, 147 (2022).